



Sound velocity in severely deformed aluminum alloys: AA1100 and AA2024

Farhad Yaghoubi¹ · Saeed Khani Moghanaki¹ · Mohsen Kazeminezhad¹

Received: 5 January 2020 / Accepted: 20 March 2020 / Published online: 30 March 2020
© Springer-Verlag GmbH Germany, part of Springer Nature 2020

Abstract

The effects of severe plastic deformation on properties of AA1100 and AA2024 including the ultrasound velocity and the shear strength during multi-axial compression (MAC) are studied. Additionally, optical microscopy, scanning electron microscopy, and X-ray energy-dispersive spectroscopy are utilized. For both AA1100 and AA2024, an opposite trend is reported in the shear strength and the sound velocity versus deformation strain of MAC. At high strain range, AA1100 and AA2024 samples reach a plateau in the strength due to the occurrence of dynamic recovery. On the other hand, the sound velocity is shown to decrease 11% and 15% for AA1100 and AA2024, respectively. Furthermore, the microstructural evaluation reveals that during severe plastic deformation, grain refining for both aluminum alloys occurs. Remarkably, elongated precipitates for severely deformed AA2024 samples are observed. Both an increase in grains boundaries followed by grain refining and elongated precipitates contribute to ultrasonic wave scattering. The presence of such scattering sites is responsible for a noticeable decrease in sound velocity.

Keywords Severe plastic deformation · Multi-axial compression · Ultrasound velocity · Microstructure · Aluminum alloy

1 Introduction

Aluminum and its alloys are known as low-weight, low-cost, corrosion-resistant, and ductile metals. Among the distinct series of aluminum alloys, most of them have excellent machinability. Although aluminum alloys of 1xxx series show low strength and hardness [1], properties enhancement is possible through solid solution [2, 3], precipitation/aging [4, 5], work hardening [6], and grain refinement [7].

Introduction of severe plastic deformation (SPD) has established a mechanism for strengthening through grain refining for alloys [7]. Many investigations have paid attention to producing bulk fine-grained materials within the sub-micrometer (below 50 μm) [8] or nanometer ($< 100 \text{ nm}$) [9] range. To produce such a range of grain refinement, one can exploit multi-axial compression (MAC) [10] technology. This technology is a simple and cost-effective technology [11] among many available SPD technologies including equal-channel angular pressing (ECAP) [12], high-pressure

torsion (HPT) [13], twist extrusion (TE) [14, 15], and accumulative roll bonding (ARB) [16]. In this regard, researchers have carried out experiments on aluminum and its alloys that were processed by ECAP and MAC. As examples of such studies, one can mention [17–27] that focused on the microstructural and the mechanical properties evolution. Additionally, other categories of metals have been subjected to SPD, including pure copper [28–30], pure titanium [31], magnesium alloy [32, 33], and steel [34–36].

Fewer studies have been conducted on the properties of ultrasonic elastic waves in SPDed materials. An instance of the properties of ultrasonic waves is sound velocity. Sound velocity has been shown to evolve during plastic deformation [37–42]. Discussion on the properties of ultrasonic waves is supported by a simple principle of physics that says a medium through which the wave travels has an influence on the motion of wave [37]. That principle can be represented by the Granato and Lücke string model. Based on the string model, the ultrasonic attenuation, which is related to sound velocity, appears due to the mobility of dislocation [43, 44]. Also, Mujica et al. [45] showed the effect of dislocation density on a decrease in sound velocity for pure aluminum. Additionally, it is found that ultrasonic wave is sensitive to microstructural features such as grain

✉ Mohsen Kazeminezhad
mkazemi@sharif.edu

¹ Department of Materials Science and Engineering, Sharif University of Technology, Azadi Avenue, Tehran, Iran

boundary [46] and distortion direction [47], precipitations [48], deformation twins [49], and texture and point defects [50]. Although remarkable studies have been conducted, all the mentioned researches are limited to small plastic-strained alloys, and before necking point.

This study aims to measure elastic wave velocity in samples that have experienced high/severe plastic strain. The relation between ultimate shear strength, microstructural, and sound velocity evolution is investigated during the MAC process in 1xxx and 2xxx series aluminum alloys. Furthermore, we consider the effect of second-phase particles on sound velocity.

2 Experimental procedures

2.1 Sample preparation

The chemical compositions of the investigated aluminum alloys are summarized in Table 1. The samples were cut into $10 \times 10 \times 15 \text{ mm}^3$ rectangular prisms. The AA1100 samples were annealed in an electrical resistance furnace at 673 K for 2 h and then cooled in air. The AA2024 samples were solution-treated in an electrical resistance furnace at 768 K for 2 h and then quenched in water. For overaging purpose, the quenched alloys were held at 573 K for 1 h and then cooled in the furnace.

The samples were placed into the cavity of a die to apply MAC process. The rectangular prisms were compressed at room temperature through the various passes that are illustrated schematically in Fig. 1. Disulfide molybdenum (MoS_2) lubricant agent was applied to the surfaces of samples and die wall to minimize the friction during the process. The sample was rotated by 90° after each pass and re-inserted into the die such that the smallest dimension of 10 mm fits in the width of the die channel. The compression force was only applied on the surfaces 1 and 3 alternatively,

and the ram speed was 1 mm/s. The samples experienced the equivalent strain of $\varepsilon = 2/\sqrt{3} \ln(W/H)$ during each pass, where H is the height of the sample ($= 15 \text{ mm}$) and W is the width of the sample ($= 10 \text{ mm}$) [51]. In this study, one, three, five, and seven passes were applied to the samples (corresponding equivalent strains of 0.47, 1.41, 2.35, and 3.29).

2.2 Sound velocity measurement

Longitudinal sound velocity was measured according to ASTM standard E 494-99 by using a Trusonic Plus EN12668-1 compliance ultrasonic flaw detector. The sound velocity calculation was based on the pulse echo method. In this method, near-field effect does not influence the results of sound velocity measurements because one wave has left the detector before the next one is received by the detector. The calibration standard block VI was used to calibrate the equipment. A 4 MHz longitudinal beam probe with a diameter of 8 mm was used to measure sound velocity, and filtered machine oil was used as the couplant for the longitudinal wave probe. Since the samples exhibited slightly irregular shape after each compression step, they were polished to have smooth, flat, and parallel surfaces. The temperature affects the measurement; therefore, the temperature was kept the same for all the specimens. The mean values for the velocities were obtained by averaging three independent measurements.

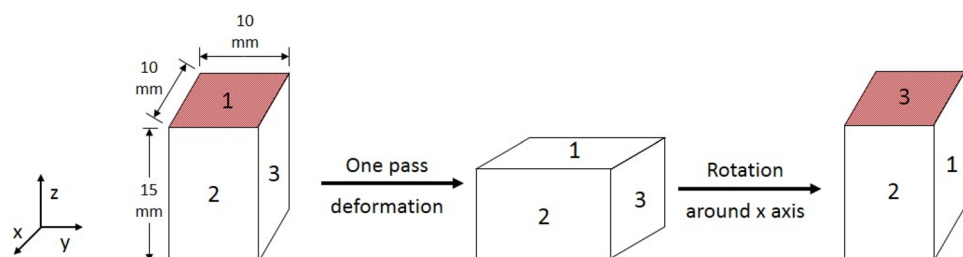
2.3 Microstructural examination

The microstructural observations were exactly conducted into equally half along the compression axis and the cross section. As a result, we can correlate sound velocity measurements to the microstructure of the section along which the longitudinal waves pass. Each of the deformed samples was cut along the midline of the long side and then

Table 1 Chemical composition of investigated AA1100 and AA2024 (wt%)

| | Al | Si | Fe | Cu | Mn | Mg | Cr | Ni | Zn |
|--------|------|----------------|-------|------|-------|------|--------|--------|-------|
| AA1100 | Base | 0.95 (Si + Fe) | | 0.20 | 0.05 | – | – | – | 0.1 |
| AA2024 | Base | 0.112 | 0.348 | 3.86 | 0.449 | 1.23 | 0.0195 | 0.0172 | 0.297 |

Fig. 1 The schematic of the MAC process



mechanically polished. For the next step, the microstructure of AA1100 samples was revealed by electro-etching with Barker's solution (2.5% HBF_4 in 100 ml H_2O) at 20 V and 22 A. Additionally, the microstructure of AA2024 samples was revealed by etching with a diluted solution of 10 g sodium hydroxide (NaOH) and 5 g potassium ferrocyanide (K_4FeCN) in 100 cc H_2O . Microstructural examinations were carried out by an optical polarized light microscope Olympus PME3. Moreover, the precipitates were investigated in mechanically polished AA2024 samples with a field-emission scanning electron microscope at the operating voltage of 15 kV. Also, X-ray diffraction (XRD) analysis was carried out using a PANalytical diffractometer with $\text{Cu K}\alpha$ radiation at 50 steps per degree to investigate precipitates in the overaged AA2024 samples.

2.4 Shear strength measurement

Small square specimens of 10 mm sideway and 1.0 mm thickness was cut from the severely deformed AA1100 and AA2024 specimens. The surfaces of the specimens were ground using SiC papers and were polished to a final thickness in the range of 0.75–0.8 mm. A shear punch test was carried out using a Hounsfield test machine at room temperature and a constant crosshead speed of 0.25 mm/min. The load–displacement data which was obtained by a shear punch test (SPT) was converted into shear stress (τ) and normalized displacement (δ) by the following expressions [52]:

$$\tau = P/2\pi r t \quad (1)$$

$$\delta = d/t \quad (2)$$

where P is the applied load, t is the specimen thickness (= 0.75–0.8 mm), r is the average of punch and lower die radius (= 6 mm), and d is the displacement of punch. Normalized displacement is the displacement of the punch, which is normalized by the thickness of the specimen.

3 Results and discussion

3.1 Microstructure

Figures 2 and 3 demonstrate the microstructures of aluminum alloys AA1100 and AA 2024 during the MAC process, respectively. Figure 2a shows that the annealed AA1100 sample contains both fine and coarse grains. After one pass, a few elongated grains are observed (Fig. 2b). In the microstructure of the third pass sample, a significant number of coarse elongated grains in addition to the fine

grains are observed (Fig. 2c). Formation of round-shaped grains is noticeable besides a few elongated ones for five passes (Fig. 2d). Interestingly, there is a considerable amount of deformation bands forming within the grains (Fig. 2f). Additionally, for approximately the same strained sample, Yang et al. [22] argued that the elongated grains shortened by transverse boundaries can be accounted for the formation of equiaxed grains. Moreover, a likely cause for the presence of large grains in Fig. 2d is deformation-induced grain growth. Grain growth takes place through grain rotation and grain boundary migration, in the case of nanocrystalline grains and grains larger than 100 nm, respectively [53, 54]. By further deformation, fine elongated grains are still formed after seven passes of MAC (Fig. 2e).

As shown in Fig. 3a, for AA2024, coarse grains are observed in the overaged sample. Figure 3b shows fine grains that are formed in the center and elongated ones at the edge of the sample. In Fig. 3c, more elongated grains oriented perpendicular to elongated ones at sides of the sample are observed after three passes. By further deformation (Fig. 3d), the grain refinement occurs remarkably in the center and extends toward the sides of the sample. Also, it can be seen that some coarse grains are divided into fine grains (Fig. 3e).

In Fig. 4a, spherical and dispersed precipitates are shown for the overaged AA2024 sample. Additionally, by exposing samples to severe deformation, elongated precipitates are formed as it is revealed for seven passes (Fig. 4b). The intermetallic precipitates, according to the elemental map (Fig. 5), are mostly composed of Al, Cu, and Fe. These intermetallic particles are formed during solidification, and they are mainly $\text{Al}_7\text{Cu}_2\text{Fe}$. The XRD analysis of the overaged AA2024 (Fig. 6) also indicates the presence of $\text{Al}_7\text{Cu}_2\text{Fe}$ intermetallic particles. Moreover, there are some peaks which are related to Al_2CuMg particles formed during the overaging process. The (111) and (200) peaks refer to the aluminum matrix.

3.2 Ultimate shear strength

Figures 7 and 8 show the ultimate shear strength evolution of AA1100 and AA2024 samples versus the number of MAC passes, respectively. According to Fig. 7, the strength is increased from 67 to 91 MPa for the annealed sample after three passes of MAC. However, shear strength turns relatively unchanging upon further deformation. For AA2024 specimens (Fig. 8), the strength rises more than 70 MPa from 139 MPa after the one pass; then, it reaches the maximum value of 211 MPa after three passes. Although the strength varies erratically for five and seven

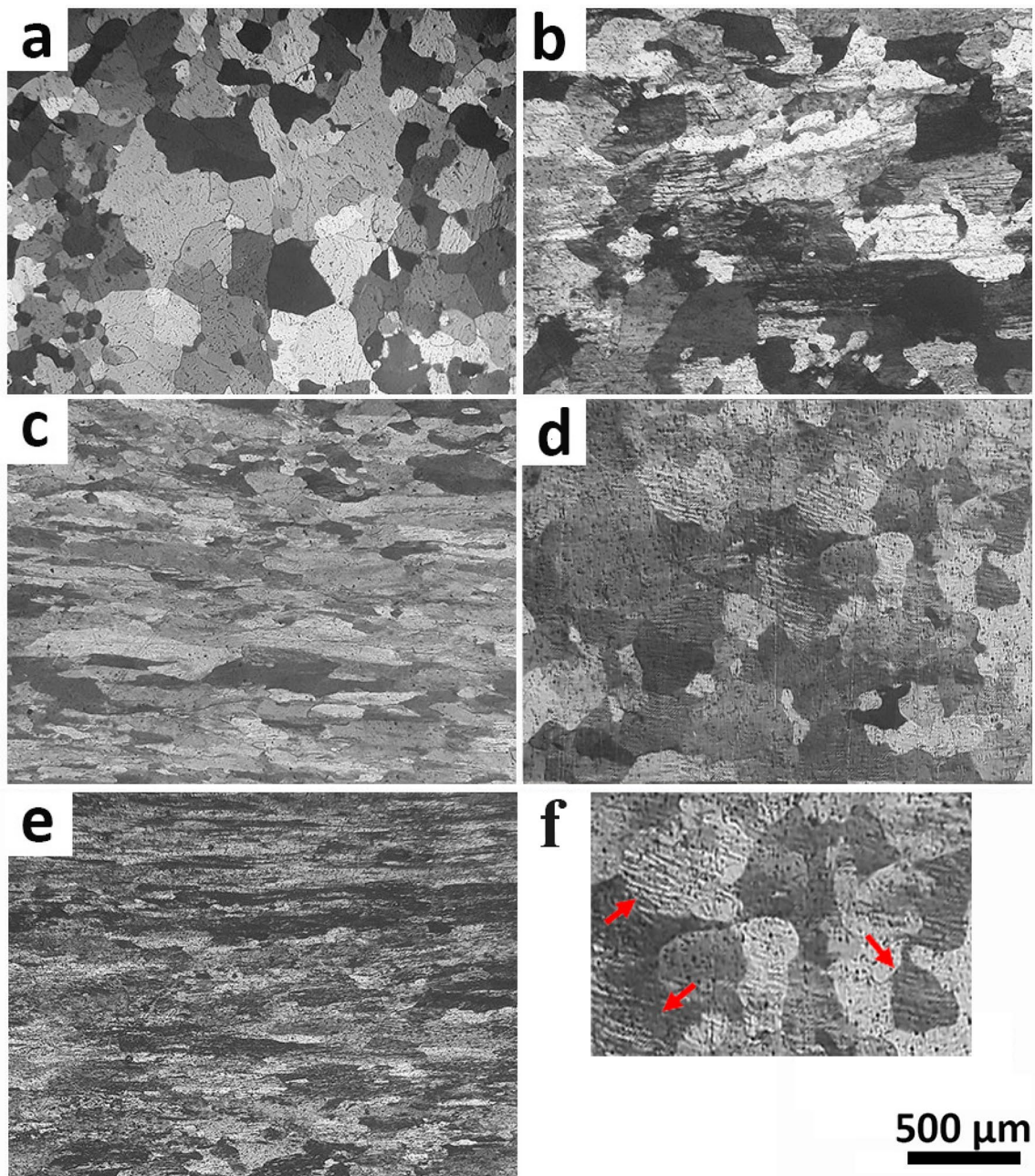


Fig. 2 Microstructure of AA1100 samples; **a** annealed, **b** one-, **c** three-, **d** five-, **e** seven-, **f** five-pass sample at larger magnification

passes, its variation is almost constant compared with those of the initial passes.

For AA1100, the considerable increase in strength at low strains (one and three passes) can be linked to both contributions of the grain refining phenomenon and the multiplication of dislocations based on the Frank–Read mechanism. Nevertheless, the shear strength stops rising

after three passes due to dynamic recovery [19, 22]. For AA2024, the Mg solute atoms affect the strength of Al in two ways. Firstly, at low strains, dislocations are pinned, and their motion is made slow. Secondly, the annihilation of dislocations becomes difficult during deformation. As a result, the dislocation density is indirectly increased [55]. Furthermore, the grain growth is impeded by the solute atoms dragging and fine precipitates like S/S (Al_2CuMg) phases.

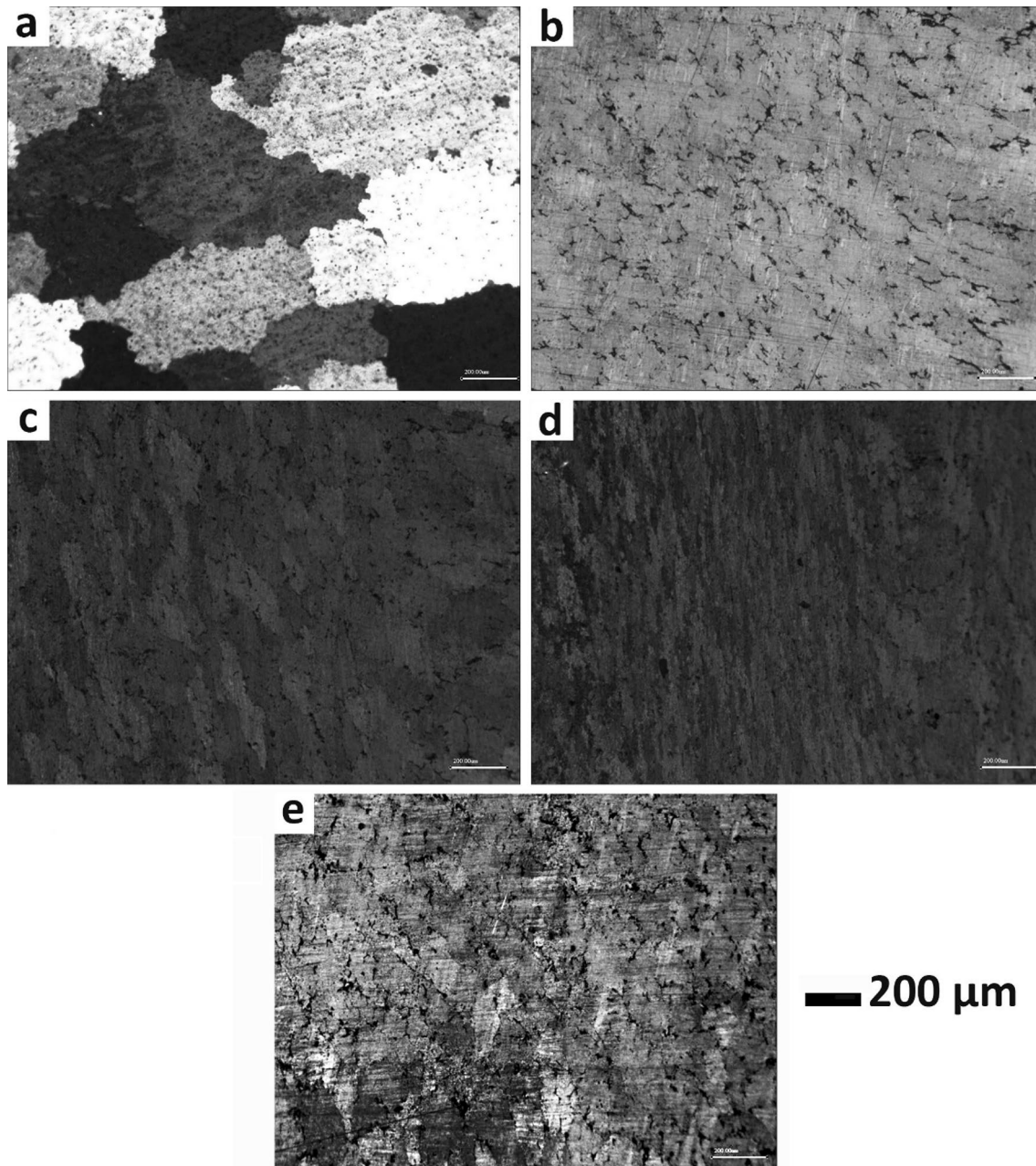


Fig. 3 Microstructure of AA2024 samples: **a** overaged, **b** one-, **c** three-, **d** five-, **e** seven-pass samples

3.3 Sound velocity measurement

In Figs. 9 and 10, the changes in the sound velocity of AA1100 and AA2024 (4 MHz longitude wave probe) are presented as a function of MAC passes, respectively. The sound velocity of the alloys has a trend contrary to the trend of the shear strength. For AA1100, the velocity is gradually decreased from 6557 to 6543 m/s at low strains, and then, the velocity plunges 8.3% after three passes. Finally, the velocity levels out at around 5900 m/s corresponding to 10% decline compared with the velocity of the annealed

sample. For AA2024, the velocity reduces about 100 m/s to 6625 m/s for one pass. Contrary to AA1100, the decrease in sound velocity continues as the plastic deformation becomes more severe in AA2024. Up to seven passes (a strain of ~ 3.3), the velocity falls to $\sim 15\%$ lower velocity compared with the initial value that is 6722 m/s.

For AA1100, as discussed in a similar study for pure copper [56], dislocations—as a result of plastic deformation—influence on a propagating wave across a solid. Therefore, the greater dislocation density results in a more wave absorption realized by a decrease in the velocity of the

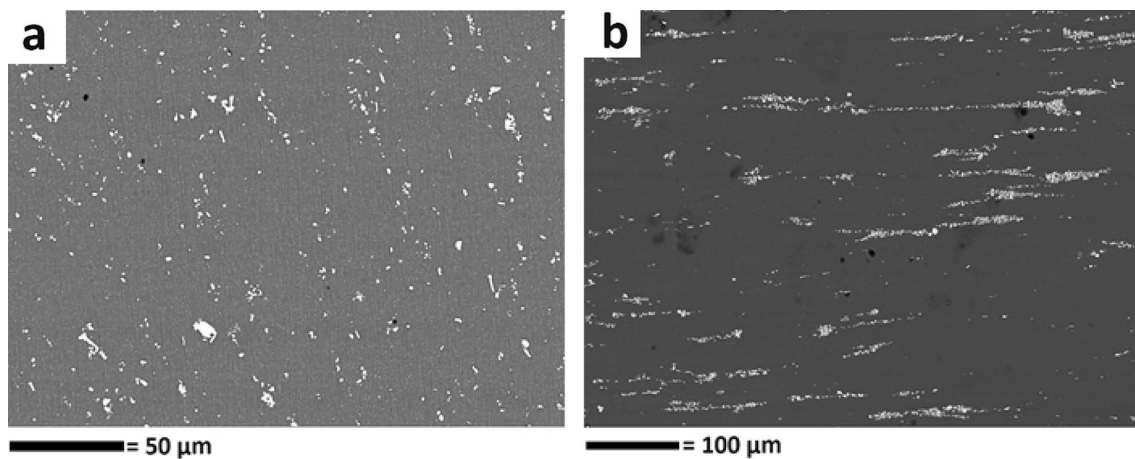


Fig. 4 SEM micrographs of **a** overaged AA2024 sample without deformation and **b** overaged AA2024 sample subjected to MAC for seven passes

wave. This theory was discussed in both elastic and plastic regimes during tensile testing [39, 43, 44]. In addition, the presence of grain boundaries leads to further loss of energy of the ultrasound wave [46]. This share of energy loss is due to a discontinuity in elastic properties at each grain boundary [46]. Thus, the formation of fine grains also contributes to wave scattering and therefore further decrease in the velocity. In a similar manner, deformation bands, which lead to a higher level of inhomogeneity, lower sound velocity of the fifth pass sample.

Furthermore, for AA2024, besides the points mentioned about AA1100, precipitates play a key role in altering the sound velocity [48]. The difference in the elastic modulus of the phases and precipitates–matrix interface is considered as other kinds of scattering cause [48]. Therefore, the presence of precipitates can be responsible for the more noticeable decrease in the sound velocity of AA2024 than that of AA1100. In Fig. 10, although the shear strength does not change considerably at high strain stage, the velocity plunges to 5797 m/s (the lowest of its value after seven passes). According to Fig. 4b, further deformation leads to an elongated configuration of precipitates, whereas, based on Fig. 4a, the precipitates are more evenly agglomerated and dispersed. The elongated configuration is in the order of hundreds of micrometers which is relatively in the same order of the wavelength of the wave used in this study. Hence, the elongated precipitates are effective enough to scatter the propagating wave [57]. Also, the effect of elongated precipitates on sound velocity was studied similarly but for grain distortion in cold-formed aluminum profile by Keran et al. [47].

4 Conclusions

SPD has shown itself as one of the most promising processes giving rise to further enhancement in materials properties. In addition to mechanical properties that have been appreciably investigated by recent research, sound propagation properties in materials can be improved by SPD process. As an instance, vibration dissipation and noise cancelation count as applications of the sound propagation properties.

The utilized method in this study provides results that are useful to study the correlation between sound velocity and mechanical properties such as materials' strength, damping, or other acoustical parameters. Although this method is simple and nondestructive, distorted shape and surface condition of SPDed samples are problematic for ultrasonic measurements.

In summary, the effect of SPD on the sound velocity and shear strength of aluminum alloys was investigated and the following conclusions can be drawn:

1. Microstructural observation reveals grain refining. Moreover, in AA 2024 case, the elongated precipitates are formed. These microstructural features lead to measure an increase in the strength and a decrease in the sound velocity as a function of MAC passes.
2. The values of shear strength and sound velocity show the opposite trend.
3. Both AA1100 and AA2024 show 24 and 70 MPa increase in shear strength until three passes of MAC,

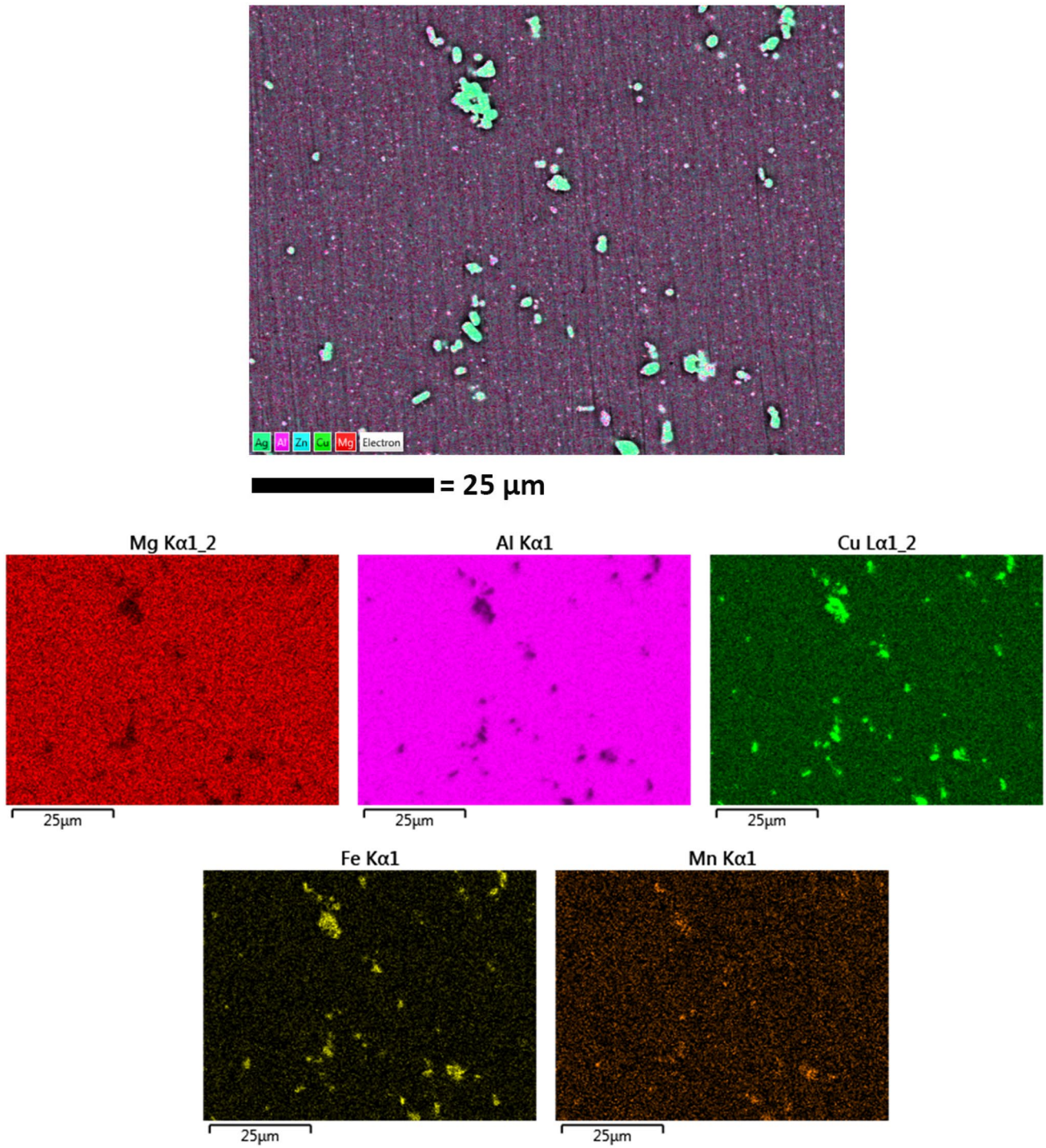


Fig. 5 Elemental map of overaged AA2024 sample

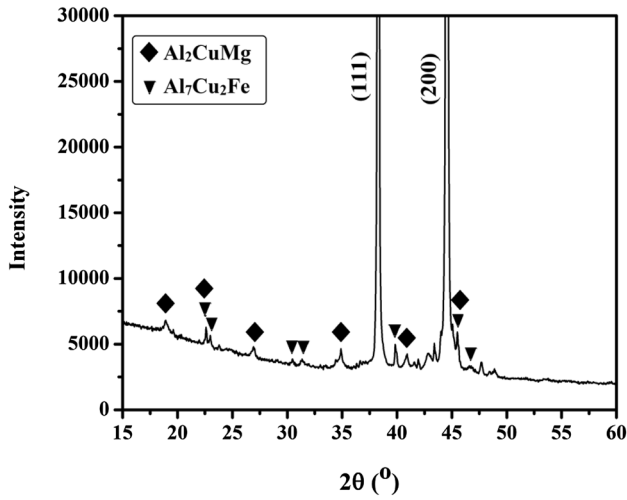


Fig. 6 The XRD analysis of overaged AA2024 sample

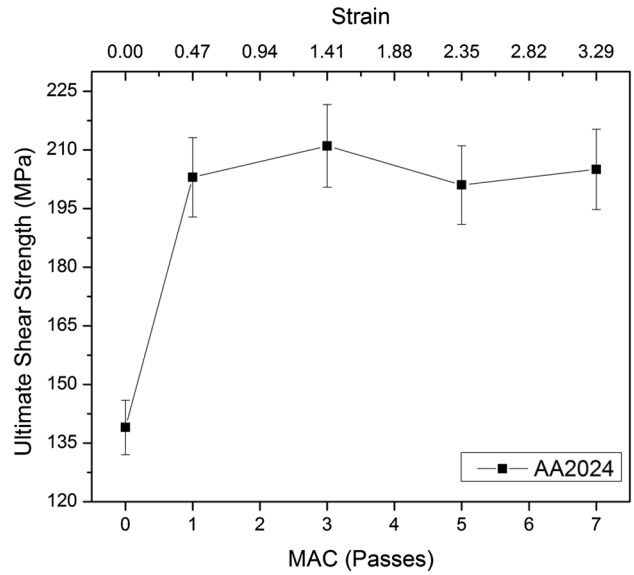


Fig. 8 Ultimate shear strength of overaged AA2024 samples during the MAC process

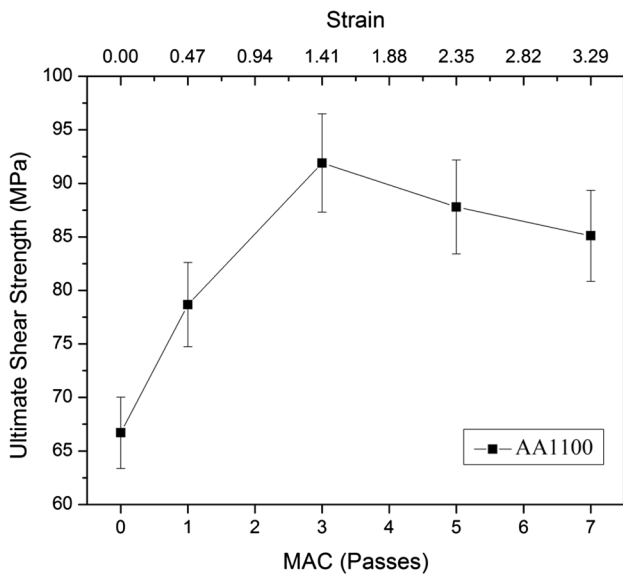


Fig. 7 Ultimate shear strength of AA1100 samples during the MAC process

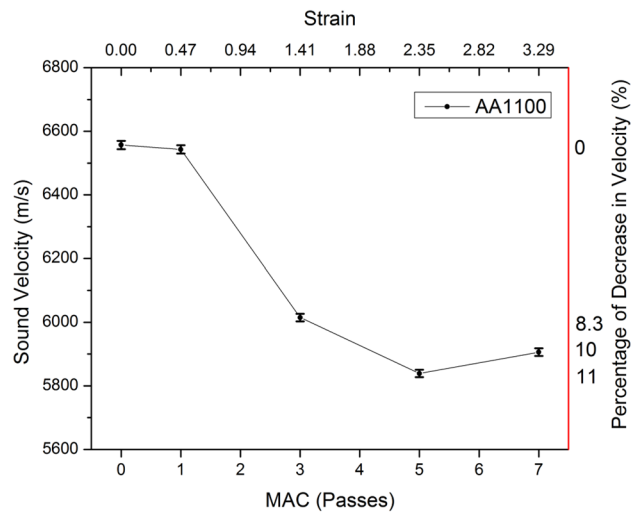


Fig. 9 Sound velocity evolution in AA1100 samples as a function of MAC passes

respectively. Then, due to dynamic recovery, the strength flattens out for both aluminum alloys.

4. Furthermore, despite a downward trend in the sound velocity for both studied aluminum alloys, the velocity is increased by about 60 m/s after the strain of 2.37

for AA1100 samples. Dynamic recovery is responsible for this slight increase in the velocity. In contrast, the continuous decrease in the velocity for AA2024 specimens is attributed to the presence of elongated precipitates.

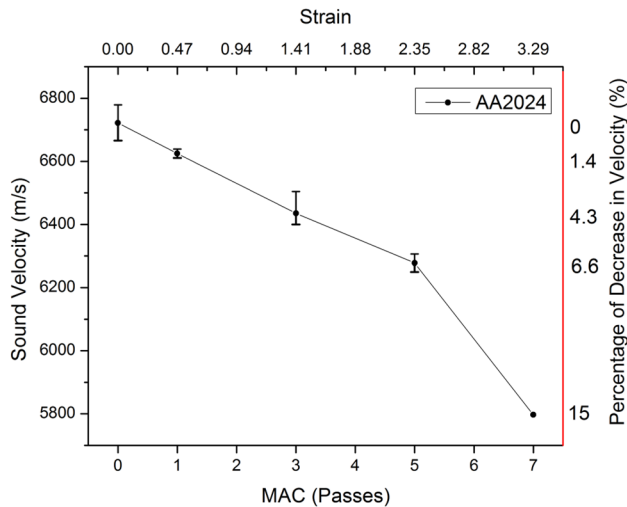


Fig. 10 Sound velocity evolution in overaged AA2024 as a function of MAC passes

Acknowledgements The authors wish to thank the Research Board of Sharif University of Technology, Iran, and Prof. Movahedi and Prof. Aashuri for provision of the research facilities used in this work.

References

- P.J. Blau, J.R. Davis, *Nonferrous alloys and special-purpose materials* (ASM Handbook, Materials Park, 2000), pp. 222–483
- Q. Zhao, B. Holmedal, *Mater. Sci. Eng. A* **563**, 147–151 (2013)
- H. Shang, B. Ma, K. Shi, R. Li, G. Li, *Mater. Lett.* **192**, 104–106 (2017)
- T. Dorin, F. De Geuser, W. Lefebvre, C. Sigli, A. Deschamps, *Mater. Sci. Eng. A* **605**, 119–126 (2014)
- N.D. Alexopoulos, Z. Velonaki, C.I. Stergiou, S.K. Kourkoulis, *Mater. Sci. Eng. A* **700**, 457–467 (2017)
- Z. Wang, H. Li, F. Miao, B. Fang, R. Song, Z. Zheng, *Mater. Sci. Eng. A* **607**, 313–317 (2014)
- T.C. Lowe, *JOM* **58**, 28–32 (2006)
- I. Sabirov, Y. Estrin, M.R. Barnett, I. Timokhina, P.D. Hodgson, *Scr. Mater.* **58**, 163–166 (2008)
- R.Z. Valiev, R.K. Islamgaliev, I.V. Alexandrov, *Prog. Mater. Sci.* **45**, 103–189 (2000)
- C. Granato, N. Almeida, M. Aguilar, P. Cetlin, *Mater. Lett.* **174**, 153–156 (2016)
- S.V. Zherebtsov, G.A. Salishchev, R.M. Galeev, O.R. Valiakhmetov, S.Yu. Mironov, S.L. Semiatin, *Scr. Mater.* **51**, 1147–1151 (2004)
- S. Ghosh, C. Xu, T.G. Langdon, *Mater. Sci. Eng. A* **473**, 219–225 (2008)
- A.P. Zhilyaev, T.G. Langdon, *Prog. Mater. Sci.* **53**, 893–979 (2008)
- M.I. Latypov, I.V. Alexandrov, Y.E. Beygelzimer, S. Lee, H.S. Kim, *Comput. Mater. Sci.* **60**, 194–200 (2012)
- D. Orlov, Y. Beygelzimer, S. Synkov, V. Varyukhin, N. Tsuji, Z. Horita, *Mater. Sci. Eng. A* **519**, 105–111 (2009)
- Y. Saito, N. Tsuji, H. Utsunomiya, T. Sakai, R. Hong, *Scr. Mater.* **39**, 1221–1227 (1998)
- R.Z. Valiev, T.G. Langdon, *Prog. Mater. Sci.* **51**, 881–981 (2006)
- M. Ferry, F. Humphreys, *Acta Mater.* **44**, 3089–3103 (1996)
- R. Kapoor, A. Sarkar, R. Yogi, S.K. Shekhawat, I. Samajdar, J.K. Chakravarty, *Mater. Sci. Eng. A* **560**, 404–412 (2013)
- X. Xu, Q. Zhang, N. Hu, Y. Huang, T.G. Langdon, *Mater. Sci. Eng. A* **588**, 280–287 (2013)
- M. Montazeri-Pour, M.H. Parsa, H.R. Jafarian, S. Taieban, *Mater. Sci. Eng. A* **639**, 705–716 (2015)
- X. Yang, D. Wang, Z. Wu, J. Yi, S. Ni, Y. Du, M. Song, *Mater. Sci. Eng. A* **658**, 16–27 (2016)
- Q.F. Zhu, L. Li, C.Y. Ban, Z.H. Zhao, Y.B. Zuo, J.Z. Cui, *Trans. Nonferrous Met. Soc. China* **24**, 1301–1306 (2014)
- L.F. Pan, L. Chen, W.L. Yan, *Adv. Mater. Res.* **1064**, 26–31 (2014)
- K. Rodak, K. Radwański, R.M. Molak, *Solid State Phenom.* **176**, 21–28 (2011)
- W. Yan, X. Liu, J. Huang, L. Chen, *Mater. Des.* **49**, 520–524 (2013)
- W.C. Liu, M.B. Chen, H. Yuan, *Mater. Sci. Eng. A* **528**, 5405–5410 (2011)
- A. Takayama, X. Yang, H. Miura, T. Sakai, *Mater. Sci. Eng. A* **478**, 221–228 (2008)
- A. Kundu, R. Kapoor, R. Tewari, J.K. Chakravarty, *Scr. Mater.* **478**, 221–228 (2008)
- T. Sakai, H. Miura, X. Yang, *Mater. Sci. Eng. A* **499**, 2–6 (2009)
- B. Wang, J. Li, J. Sun, X. Wang, Z. Liu, *Mater. Sci. Eng. A* **612**, 227–235 (2014)
- Y. Xu-yue, S.U.N. Zheng-yan, X. Jie, *Trans. Nonferrous Met. Soc. China* **18**, 200–204 (2008)
- W. Gan, H. Brokmeier, M. Zheng, K. Wu, *Adv. Mater. Res.* **147**, 879–882 (2010)
- H. Miura, H. Hamaji, T. Sakai, T. Fujita, N. Yushinaga, *Mater. Sci. Forum* **503–504**, 293–298 (2006)
- A. Bhowmik, S. Biswas, S.S. Dhinwal, A. Sarkar, R.K. Ray, D. Bhattacharjee, *Mater. Sci. Forum* **703**, 774–777 (2011)
- V. Soleymani, B. Eghbali, *J. Iron. Steel Res. Int.* **19**, 74–78 (2012)
- S.H.Á. Tang, J.W. Hao, H.L. Pan, *NDT E Int.* **40**, 486–495 (2007)
- L.B. Zuev, B.S. Semukhin, K.I. Bushmelyova, N.V. Zarkovskaya, *Mater. Lett.* **42**, 97–101 (2000)
- X. Min, H. Kato, N. Narisawa, K. Kageyama, *Mater. Sci. Eng. A* **392**, 87–93 (2005)
- A. Hikata, B. Chick, C. Elbaum, R. Truell, *Acta Mater.* **10**, 423–429 (1962)
- E.R. Naimon, M. Ledbetter, W.F. Weston, *J. Mater. Sci.* **10**, 1309–1316 (1975)
- M. Taniguchi, Y. Iwashimizu, *Ultrasonics* **25**, 160–165 (1987)
- A. Granato, K. Lucke, *J. Appl. Phys.* **27**, 583–593 (1956)
- A. Granato, A. Hikata, *Acta Metall.* **6**, 470–480 (1958)
- F. Lund, N. Mujica, M.T. Cerda, R. Espinoza, J. Lisoni, *Acta Mater.* **60**, 5828–5837 (2012)
- R.B. Thompson, F.J. Margetan, P. Haldipur, L. Yu, A. Li, P. Panetta, H. Wasan, *Wave Motion* **7**, 1–7 (2016)
- Z. Keran, M. Mihaljevi, B. Runje, D. Marku, *Arch. Civ. Mech. Eng.* **17**, 375–381 (2017)
- F. Tariq, N. Naz, R. Ahmed, *J. Nondestructive Eval.* **31**, 17–33 (2012)
- H. Watanabe, Y. Sasakura, N. Ikeo, T. Mukai, *J. Alloys Compd.* **626**, 60–64 (2015)
- S.H. Tang, S. Wu, M. Kobayashi, H.L. Pan, *Int. J. Solids Struct.* **44**, 1277–1290 (2007)
- A. Azushima, R. Kopp, A. Korhonen, D.Y. Yang, F. Micari, G.D. Lahoti, P. Groche, J. Yanagimoto, N. Tsuji, A. Rosochowski, A. Yanagida, *CIRP Ann. Manuf. Tech.* **57**, 716–735 (2008)

52. S. Emami Kervee, P. Pourshayan, F. Nasrollahnezhad, S.K. Moghanaki, M. Kazeminezhad, R.E. Logé, S. Nobakht, *Mater. Sci. Tech.* **34**, 688–697 (2018)
53. Y.B. Wang, J.C. Ho, X.Z. Liao, H.Q. Li, S.P. Ringer, Y.T. Zhu, *Appl. Phys. Lett.* **94**, 011908 (2009)
54. M. Legros, D.S. Gianola, K.J. Hemker, *Acta Mater.* **56**, 3380–3393 (2008)
55. J. Gubicza, N.Q. Chinh, Z. Horita, T.G. Langdon, *Mater. Sci. Eng. A* **389**, 55–59 (2004)
56. H. Schmidt, D. Lenz, E. Drescher, K. Lucke, *J. Phys. Colloques* **42**, 339–344 (1981)
57. B. Raj, V. Moorthy, T. Jayakumar, K.B.S. Rao, *Int. Mater. Rev.* **48**, 273–325 (2003)

Publisher's Note Springer Nature remains neutral with regard to jurisdictional claims in published maps and institutional affiliations.